

Article

Exploring Promising Catalysts for Chemical Hydrogen Storage in Ammonia Borane: A Density Functional Theory Study

Sateesh Bandaru ^{1,2,3,*}, Niall J. English ^{1,2,*}, Andrew D. Phillips ^{1,4} and J. M. Don MacElroy ^{1,2}

¹ The SFI Strategic Research Cluster in Solar Energy Conversion, University College Dublin, Belfield, Dublin 4, Ireland; andrew.phillips@ucd.ie (A.D.P.); don.macelroy@ucd.ie (J.M.D.M.)

² School of Chemical and Bioprocess Engineering, University College Dublin, Belfield, Dublin 4, Ireland

³ Beijing Computational Science Research Centre, Beijing 100193, China

⁴ School of Chemistry and Chemical Biology, University College Dublin, Belfield, Dublin 4, Ireland

* Correspondence: patrudu_iict@csrc.ac.cn (S.B.); niall.english@ucd.ie (N.J.E.);

Tel.: +86-10-56981938 (S.B.); +356-1-7161646 (N.J.E.)

Academic Editors: Albert Demonceau, Ileana Dragutan and Valerian Dragutan

Received: 20 October 2016; Accepted: 21 April 2017; Published: 5 May 2017

Abstract: Density functional theory (DFT) has been applied to study potential ammonia borane (AB) dehydrogenation pathways via new bifunctional ruthenium-based catalysts, alongside their computationally-designed iron-based counterparts (i.e., four catalysts), using the wB97XD (dispersion-included) functional. The efficiency of each catalyst was under scrutiny based on the addition of ammonia borane, with a focus on the associated activation-energy barriers, whilst hydrogen release from the catalyst was also studied in detail. Here, natural-population analysis charges were key quantities of interest. It was found that the iron-based catalysts display more promising dehydrogenation energy barriers vis-à-vis their Ru-based counterparts, and that ammonia-borane addition to the metal catalyst is more energetically favorable than dehydrogenation.

Keywords: ammonia borane; density functional theory; metal catalysis; hydrogen storage

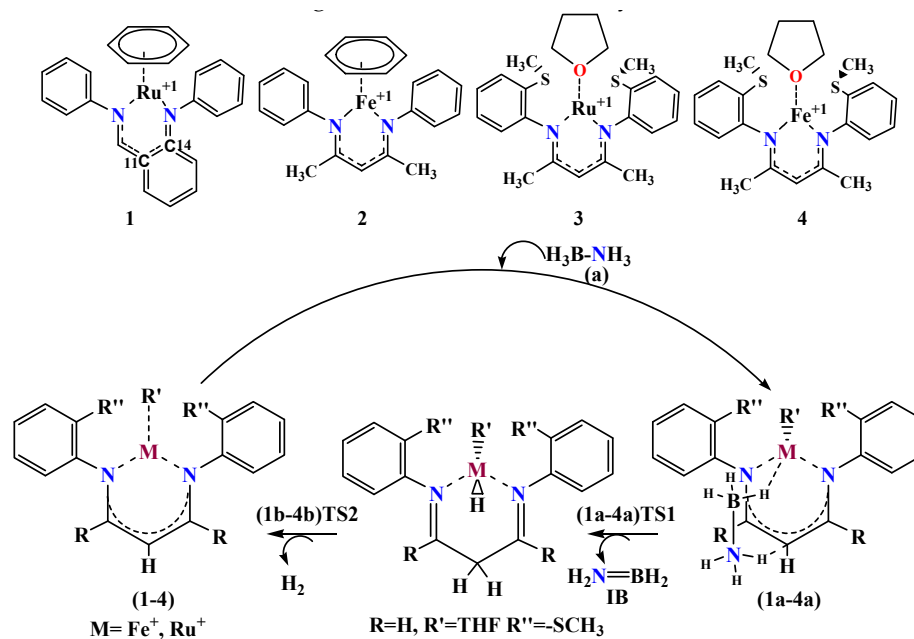
1. Introduction

There is a litany of formidable obstacles to be overcome in order to realize the Hydrogen Economy; indeed, the chemical storage of hydrogen is a potentially rewarding strategy [1,2]. Ammonia borane (AB) (and associated amine borane analogues) have been advanced relatively recently as potentially attractive and effective materials for hydrogen storage, in no small part due to simultaneously high densities on both their gravimetric (19.6 wt % H₂) and volumetric bases [1,2]. Thermal dehydrogenation of an ammonia borane molecule yields one H₂ equivalent as well as an amino borane (polymeric) product; the activation energy barrier of this process is ~36 kcal/mol [1,2]. Therefore, efficient catalysts are needed to afford hydrogen release from ammonia borane and analogues. Indeed, the release of H₂ from AB and related substrates can involve different methods, including thermal decomposition, either (i) in the solid state or (ii) in solution, (iii) hydrolysis, and catalytic dehydrogenation in solution—either (iv) homogeneous or (v) heterogeneous. From an experimental perspective, the fourth approach is the most promising, because it allows for high selectivity through intimate substrate-catalyst interactions, which could ultimately allow for controllable and reversible processes. Experimentally, homogeneous transition-metal-catalyzed dehydrogenation of amine boranes has been undertaken, and a number of highly potent catalysts have been developed. In all of these cases, experimental reports have shown rapid release of 1 equivalent of H₂ from AB only. Therefore, we are closely observing experimental progress, and working with experimentalists, wherever possible; our computational studies focus on releasing 1 equivalent of hydrogen only.

There are many published theoretical and experimental studies on the dehydrogenation of ammonia-borane [3–17] in both solution as well as the solid state. These studies demonstrate that reactions featuring transition-metal and s-block metal-centered-complex catalysts facilitate an efficient lower-temperature release of hydrogen. Many experiments have examined dehydrogenation of ammonia borane catalyzed by acids [6,7] and transition metals [8–11]; dehydrogenation in materials based on ionic liquids has also been highlighted recently [12]. Balazs et al. have rationalized the differences in dehydrogenation between ammonia- and phosphine-boranes from both experimental and theoretical standpoints [13]. Swinnen et al. have performed theoretical studies of catalyzed reaction pathways for hydrogen uptake and release in ammonia boranes, hydrazine, and ammonia alane derivatives, within the framework of Density Functional Theory (DFT) [14,15]; the resultant insights are crucial in establishing key mechanisms so as to ameliorate overall reversibility and efficiency. In addition, we have studied the mechanisms underpinning **AB** dehydrogenation, facilitated by an innovative bifunctional η^6 -arene β -diketiminato ruthenium catalyst [16,17]. Boddien et al. [18,19] have examined efficient dehydrogenation of formic acid using an iron-based catalyst, highlighting DFT-based insights and experimental kinetic studies. Yan et al. [20] have developed markedly catalytic amorphous iron nanoparticles for H_2 generation from **AB**. Baker et al. have synthesized iron complexes comprising amido- and phosphine-supporting ligands, and have scrutinized the reactivity thereof [21]. In general, bifunctional iron amido complexes exhibit selectivity control, but unwanted reactivity of N-ligands.

Douglas et al. [22–25] performed experiments to dehydrogenate ammonia borane and other cyclic amino boranes using metal-mediated catalysts. Butera et al. carried out a theoretical investigation to evaluate the role of chelating phosphine rhodium complexes in dehydrocoupling reactions of amine-boranes [26]. Further, and interestingly, Butera et al. have reported DFT studies on hydrogen release from dialkylamine-boranes enhanced via Mg and Ca complexes [27]. Li et al. [28] have reported the catalytic mechanism for production of H_2 and CO_2 from CH_3OH and H_2O by $[K(dme)_2][Ru(H)(trop_2dad)](K(dme)_2)$, investigated by DFT calculations. At low temperatures ($<100^\circ C$), Alberico et al. [29] have reported aqueous methanol dehydrogenation to H_2 and CO_2 using the ruthenium PNP complex $(RuH(CO)Cl(HN(C_2H_4Pi-Pr_2)_2))$. Jinga et al. [30] have uncovered detailed mechanisms for the dehydrogenation of methanol-water mixtures catalyzed by ruthenium complexes.

In general, in the ammonia-borane dehydrogenation step, the energy barrier for releasing the first equivalent of H_2 from **AB** is larger than that for cleavage of the B-N bond [4]. Therefore, an efficient catalyst is needed for hydrogen transfer at fuel-cell operating temperatures. The design and synthesis of novel metal hydrogen-storage catalysts for **AB** is of continuing interest from both experimental and theoretical perspectives. The present study focuses mainly on probing optimal chemical-storage catalysts based on a bifunctional η^6 -arene β -diketiminato catalyst [16], using both iron and ruthenium as the metal centers. In our previous study (Ref. [17]), we focused only on Ru-mediated catalysis with an earlier-generation catalyst motif. Here, in the present study, we have designed four different catalysts (cf. Scheme 1): these are an organo-ruthenium complex with the β -diketiminato ligand (**1**), an organo-iron complex featuring the β -diketiminato ligand (**2**), as well as an *ortho*-substituted *thiol* ($-SCH_3$) phenyl organo-ruthenium (**3**) and iron (**4**) complexes with the β -diketiminato ligand (i.e., 2,2'-thio) present. Here, through DFT methods, we explore the mechanistic pathways and calculate the reaction-energy barriers and gauge solvent effects, extending the scope of analysis carried out on the earlier-generation Ru-based catalysts in Ref. [17].



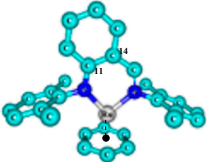
Scheme 1. Catalytic cycle for ammonia borane (AB) dehydrogenation with metal catalysts (1–4) ($R = -\text{CH}_3$).

2. Computational Details

To model dispersion with a good level of accuracy, we optimized all of the considered structures using two different DFT functionals, Truhlar's M06L [31] and Head-Gordon's wB97XD [32–35], alongside mixed basis sets in the Gaussian 09 software suite [36], using the 'Gen' keyword. Both transition metals, Ru and Fe, were modelled by Stuttgart/Dresden effective core potentials and corresponding SDDAll basis sets [37]. C, N, B, O, H atoms were treated via Pople-type [38] basis sets, i.e., 6-31 + G(d) and the S atom was handled with the aug-cc-pVTZ [39] basis set. An aug-cc-pVTZ basis set was used for S atoms, using one diffuse function for each of s, d, and p. After optimizing the geometry, frequency calculations were also performed to gauge stationary points' nature, i.e., transition states (TS) or saddle points of higher order. Unscaled zero-point energy corrections at 298 K were computed through frequency analyses with a mixed basis set of type "6-31 + G(d) + SDDAll". For all of these TS structures, an intrinsic reaction coordinate (IRC) analysis was undertaken to establish reaction pathways: here, the TS and higher-order stationary points are connected to the reactants' and products' local minima. Charge analysis was performed via 'Natural Population Analysis' (NPA) [40] using the wB97XD functional. The effect of tetrahydrofuran (THF) solvent was mimicked by the PCM continuum model [41,42] (with a static reaction-field-style [43,44] dielectric constant of 7.58) using single-point energy calculations on gas-phase-optimized geometries.

In order to validate the two functionals used, X-ray crystal parameters were used to reference the bond lengths and angles for structure 1 for five different functionals. Here, for handling transition metals, SDDAll and the C, N, B, O, and H atoms were treated with Pople basis sets, i.e., 6-311++G(d,p), and S was modelled using the aug-cc-pVTZ [39] basis set. The computed parameters are listed in Table 1. For complex 1, respective Ru-N and Ru-C^{cent} distances of 2.044 and 1.692 Å for M06L and 2.032 and 1.748 Å with wB97XD were calculated, which are in good accord with the corresponding respective experimental values of 2.021 and 1.730 Å. Bond angles were also reproduced accurately, apart from $\angle \text{Ru-N}^{\text{cent}}\text{-C11}$, which is overestimated by ca. 4°. Amongst these functionals, wB97XD leads to results in superior agreement with X-ray data. From this comparison, we opted for wB97XD in the rest of this study, and all subsequent calculations have been done with this functional.

Table 1. Experimentally synthesized Ru(+1) catalyst **1**, optimised using various functionals. Bond-length (Å) and bond-angle (degrees) differences from the X-ray crystal structure geometries are specified (with absolute X-ray values given in bold).

Structure	Theory	Ru-N	Ru-C ^{cent}	N-Ru-N	C ^{cent} -Ru-N ^{cent}	Ru-N ^{cent} -C14
	X-ray	2.021	1.730	88.5	178.0	174.5
	M06L	2.044	1.692	88.4	177.7	179.0
	M05-2X	2.032	1.763	88.6	177.0	178.5
	B3LYP	1.991	1.764	89.4	177.3	178.8
	B97D	2.019	1.724	89.6	177.5	179.1
	wB97XD	2.032	1.748	88.6	178.8	178.6

3. Results and Discussion

We need to explore the nature of the mechanistic pathways of four designed catalysts (cf. Scheme 1), in order to assess their effectiveness. We have computed the reaction-energy barriers and reaction energies for ammonia-borane addition and dehydrogenation (using wB97XD).

A putative reaction mechanism is depicted in Scheme 1 involving reaction initially with a metal catalysts **1** to **4**, taking the protic H⁺ and hydride species H⁻ from the **AB** and converting these into H₂. Firstly, the metal catalysts **1** to **4** associate with **AB** to form a reaction complex **1a** to **4a** via N...H and B...H through non-bonded interactions, and proton transfer takes place from the N atom of the **AB** to the carbanion site, and from the hydride ion to that on the metal site, to produce the di-hydrogen intermediate **1b** to **4b**. Finally, H₂ is released from the di-hydrogen intermediate and the catalysts **1** to **4** regenerate for the next catalytic cycle.

This mechanism is reasonably well known for **AB**'s thermal dehydrogenation. For a comparative analysis of reaction-energy barriers, calculations to determine the transition state (TS) without catalyst led to a gas-phase energy-barrier estimate for intramolecular dehydrogenation of **AB** of 37.04 kcal/mol; this is consistent with a value of 36.4 kcal/mol obtained at the CCSD(T)/CBS level of theory [4].

Phillips et al. were the first to publish a study of an organo-ruthenium complex featuring the β -diketiminato ligand [45]. Here, the more significant level of electron donation of this chelating *N,N'*-ligand, together with its relative steric bulkiness, allows for more facile isolation of a cationic coordinative unsaturated system; this strongly anionic *N,N'*-coordinated ligand leads to substantial charge transfer to the chelated metal [22]. To estimate the energetics of this **AB** dehydrogenation, we previously studied a phenyl-substituted version of the Ru-based catalyst of Refs. [16,17] instead of the 2,6-dimethylphenyl-substituted (2,6-(CH₃)₂C₆H₃) form which was employed in experimental studies [16]; this served to minimize potential further steric interactions [17].

4. Mechanism for Catalyst "1" Addition to Ammonia Borane

We have also elucidated the mechanism of the **AB**-addition reaction to the metal catalyst **1**. The optimized geometries of the catalyst and the TS for **AB** addition, together with the dihydrogen product and coupling of the dihydrogen TS, are depicted in Figure 1. Firstly, the metal catalyst **1** associates with ammonia borane, yielding "**1a**"; this is an energetically favorable process, as indicated in Figure 2. In **1a**, the primary (B)H-Ru interaction gives rise to a closest distance of 2.09 Å between **AB** and catalyst **1**. Whittlesey and co-workers found a similar (B)H-Ru interaction with a distance of 2.107 Å in a cationic Ru-xantphos hydride complex [46]. However, model **1a** exhibits a much weaker N(H)-C(β) interaction of over 2.52 Å. Here, to afford more realistic energy values, we also consider solvation effects. The closest distance between **AB** and catalyst **1** in **1a** is 1.82 Å: this may be observed clearly from a favorable reaction Gibbs free-energy value for the gas-phase formation of complex **1a** (-2.8 kcal/mol).

We conjecture that instances which exhibit diminished or higher reaction-energy barriers involving **1a-TS1** and **1b-TS2** correlate respectively with greater and lower charge separations; bearing this in mind, natural-population analysis (NPA) charges of the relevant atoms in the TSs, intermediates, and

catalysts are specified in Table 2. From consideration of the relative free energies in Figure 2, it is clear that the designed ruthenium catalyst **1** (cf. Figure 2) and previously reported ruthenium complex [17] exhibit opposing behavior. Interestingly, **AB** addition to Ru catalyst **1** is energetically more demanding in both the gas phase and in solution. Following formation of complex **1a**, the reaction progresses by consolidating the interaction between **1** and **AB**, realizing the transition state **1a-TS1** (cf. Figure 2). Here, we must point out differences between thermodynamic and kinetic concepts: the reaction energy value of -2.8 kcal/mol implies a thermodynamically favorable reaction, whilst the differing energy barriers imply differing accessible kinetics, assuming similar pre-exponential factors in an Arrhenius-like framework.

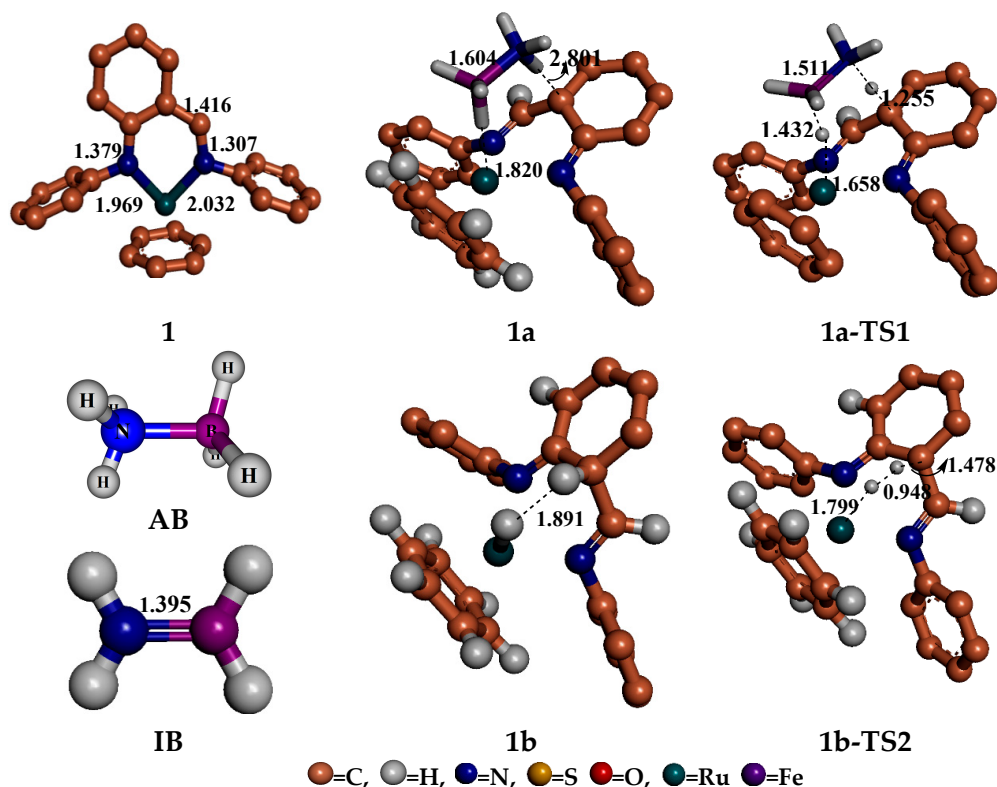


Figure 1. Significant optimized geometries of important stationary points for **AB** addition to Ru metal catalyst **1** using the wB97XD functional. Structure “**1a**” corresponds to the reaction complex and **1a-TS1** is the transition state arising from ammonia-borane addition to catalyst **1**. In this figure, only important hydrogen atoms are depicted, for greater clarity. In structure **1a**, hydrogen atoms on the benzene ring are shown, whereas in structure **1a-TS1**, benzene-ring hydrogen atoms are omitted.

In **1a-TS1** (cf. Figure 3), the two shared hydrogen atoms have shorter distances of 1.43 Å for (B)H-Ru and 1.25 Å for (N)H-C(β). Correspondingly, the B-N bond was shortened substantially to 1.51 Å. The simultaneous dual-type interaction of **1** with **AB** suggests that hydride and protic transfer from “**AB**” to “**1b**” probably occurs in a concerted manner. For gas-phase formation of “**1a**” from “**1** + **AB**”, in the first step of the potential-energy surface (PES), the computed free-energy barrier (**1a**→**1a-TS1**) was 24.2 kcal/mol, with a reaction free energy (**1a-TS1**→**1b**) of 4.5 kcal/mol. For the transition-state structure **1a-TS1**, the two shared hydrogen atoms exhibit shortened distances of 1.43 Å for (B)H-Ru and 1.25 Å for (N)H-C(β), with corresponding shortening of the B-N bond distance to 1.51 Å. The calculated energy barrier for **1a-TS1** is relative to the starting structures, i.e., catalyst **1** and ammonia borane (**AB**), and not with respect to the previous minimum **1a**.

Our whole suite of designed catalysts’ (**1**–**4**) reaction pathways, reaction-energy barriers, and reaction energies serve for ready comparison with the earlier experimentally synthesized, and

computationally analyzed, reaction mechanism of bifunctional η^6 -arene β -diketiminato ruthenium catalyst reported in Ref. [17]. Relative to findings in Ref. [17], ammonia–borane addition to ruthenium catalyst **1** is a notably higher-activation-energy process, whilst the corresponding reaction energy for the formation of the dihydrogen intermediate is also higher (cf. Figure 2). In the designed metal catalyst **1**, the β -carbon atom is more sterically hindered, because this β -carbon atom (i.e., the proton-acceptor carbon atom) is connected to the stable six-membered benzene ring (cf. Figure 1, **1**). The proton transfer from **AB**'s “NH” to the β -carbon centre alters its hybridisation from sp^2 to sp^3 (cf. Figure 1, **1b**). This process (**1a**→**1b**) appears to be more difficult and less energetically favorable.

In the case of dehydrogenation, this entails neither **AB**, nor the imino borane (IB) as a by-product, as detailed in Figure 2b; an H_2 molecule is liberated from “**1b**” via **1b-TS2** (cf. Figure 1). In the gas phase, the overall relative energy to form a hydrogenated β -diimine complex “**1b**” from “**1**” and “**AB**” is less energetically favorable; however, in the case of PCM solvation, the formation of “**1b** + **IB**” is an endothermic process. This indicates that the solvent's nature is vital for dehydrogenation of ammonia borane mediated by β -diketiminato-ruthenium complexes. This emphasizes the importance of treating solvation effects carefully [3].

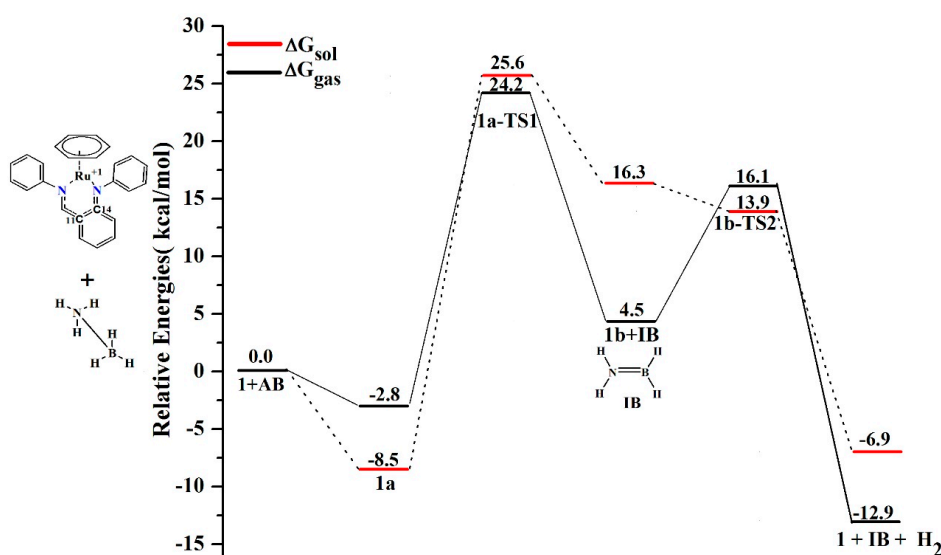


Figure 2. Profile of reaction coordinate for addition of catalyst “**1**” to “**AB**” via “**1a-TS1**”, yielding “**1b**” and H_2 release from product “**1b**”. The gas-phase relative Gibbs free energies (—) and in-solvent relative energies (---) are specified in kcal/mol.

In the mono-hydride β -diimine complex **1b**, the distance between the two hydrogen atoms is 1.891 Å; this suggests that there is some degree of interaction between these atoms ($H^{\delta+}$ and $H^{\delta-}$). The dehydrogenation of complex “**1b**” exhibits a lower energy barrier than for the **AB**-addition step; therefore, we conclude that the dehydrogenation of “**1b**” in THF is more energetically favorable than for the **AB**-addition step.

In the case of dehydrogenation/ H_2 coupling from the dihydrogen intermediate (**1b**), this step is more energetically favorable, whilst the dehydrogenation energy barrier (**1b**→**1b-TS2**) is lower than for the **AB**-addition step (**1**→**1a-TS1**) (cf. Figure 2). The dehydrogenation step is more favorable because the proton connected to the β -carbon atom associates with the sp^3 -hybridised β -carbon center with a six-membered benzene ring, and during dehydrogenation, this β -carbon center converts to the stable sp^2 -hybridised β -carbon center. The release of H_2 from the dihydrogen intermediate is more facile than for **AB** addition to **1**. Examining the NPA charges on the atoms involved in “**1b-TS2**”, the charge on the C(β) atom is negative (−0.351e). The charge accumulation on the C(β) atom disfavors the release of the proton from the C(β) atom; this rationalizes why the dehydrogenation energy barrier

was found to be higher. The difference of reaction-energy barrier can be understood clearly from charge variation on the C(β) atom, and the computed imaginary frequencies are also higher for the corresponding TS (cf. Table 2).

Table 2. Natural-population analysis (NPA) charges for wB97XD/Gen in metal catalysts “1” and “2” in reaction complexes and TSs (B, H, N, H, C, and M) and TS2 corresponding intermediate (C(β), M(Ru, Fe), H(C β), H(M)). Transition-state imaginary frequencies (ω_i) are specified in cm^{-1} .

Structure	B	H(B)	N	H(N)	C(β)	M(Ru)	ω_i
1	-	-	-	-	0.234	0.167	-
1a	-0.030	-0.027	-0.978	0.465	-0.247	0.054	-
1a-TS1	0.170	-0.007	-1.126	0.417	-0.483	-0.053	(-839.2i)
	C(β)	M(Ru)	H(Cβ)	H(Ru)	ω_i	-	-
1b	-0.413	-0.279	0.335	0.092	-	-	-
1b-TS2	-0.351	-0.099	0.228	0.024	(-1002.2i)	-	-
	B	H(B)	N	H(N)	C(β)	M(Fe)	ω_i
2	-	-	-	-	-0.352	0.297	-
2a	0.020	-0.086	-0.979	0.467	-0.481	0.371	-
2a-TS1	0.068	-0.044	-1.104	0.398	-0.653	0.307	(-1196.3i)
	C(β)	M(Fe)	H(Cβ)	H(Fe)	ω_i	-	-
2b	-0.573	-0.203	0.318	0.094	-	-	-
2b-TS2	-0.541	0.069	0.226	0.020	-648.9i	-	-

5. Mechanisms Involving Metal Catalyst “2” Addition to Ammonia Borane

In the case of organo-iron β -diketiminato ligand **2**, this catalyst has been designed based on previously-reported metal mediated organo-ruthenium metal complexes bearing the β -diketiminato ligand [17]. We have replaced the ruthenium metal center with iron, and we have considered this as a low-spin complex. The mechanism involving metal complex **2** is similar to the previously-reported ruthenium metal catalyst. In the case of the metal-modified catalyst **2**, we are interested in how the reaction energetics change from featuring a third-row transition metal to a first-row metal. All of the optimized structures and relative energy graphs are shown in Figure 3.

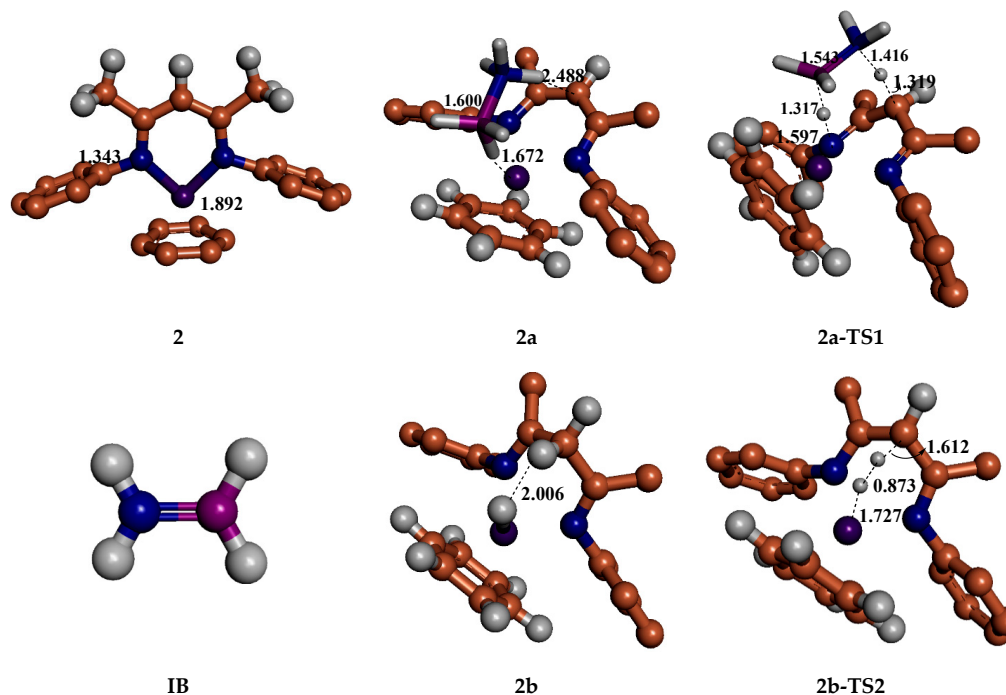


Figure 3. Significant optimized geometries of important stationary points for the reaction coordinate describing AB addition to the Fe-metal catalyst **2**. Important hydrogen atoms are highlighted.

Complex **2a**'s structure (cf. Figure 3) shows that the primary (B)H-Fe interaction gives rise to the smallest separation, 1.672 Å, between **AB** and catalyst **2**. In the association complex **2a**, **AB** is in closer contact with metal catalyst **2** compared to the reported Ru-metal association complex [17]. This can be observed clearly from the relative energy difference, in that the relative energy values are higher than for the previously-reported catalyst [17]. In contrast to the (B)H-Fe interaction, that of N(H)-C(β) is substantially weaker, with a distance of 2.48 Å. However, **2a** demonstrates an added, but markedly weaker, N(H)-C(β) interaction, giving rise to a distance of 2.48 Å. Again, solvation effects were also considered by PCM-THF treatment (shown by red bars), for more reliable energy values. Interestingly, these calculations suggest that the in-solvent formation of **2a** from the combination of **2** + **AB** is significantly less energetically demanding, with a value of -11.4 kcal/mol.

Following formation of **2a**, the reaction proceeds by enhancing the interaction between **2** and **AB**, leading to the first transition state **2a-TS1**. The reaction **2a** \rightarrow **2a-TS1** proceeds with a lower activation-energy barrier, in essentially the same manner as we reported for the earlier catalyst [17]. For the gas-phase formation of "**2a**" from "**2** + **AB**", along the first step of the PES, the computed free-energy barrier (**2a** \rightarrow **2a-TS1**) was 4.6 kcal/mol, with a reaction free energy (**1a-TS1** \rightarrow **1b**) of -13.1 kcal/mol. The formation of **2b** from the reactants (**1** + **AB** \rightarrow **2b**) is a more energetically favorable process, whilst **AB** addition for the previously reported Ru catalyst has a similar activation-energy barrier [17].

In the gas phase, the relative free energy to form a hydrogenated β -diimine complex "**2b**" from "**2**" and "**AB**" is highly energetically favorable, even in-solvent. In the case of relative-energy differences for **AB** addition in Figure 4a, these are more favorable. For the mono-hydride β -diimine complex **2b**, the separation between the two hydrogen atoms is 2.0 Å, indicating an $H^{\delta+}$ - $H^{\delta-}$ interaction. Interestingly, the dehydrogenation of complex "**2b**" exhibits a slightly higher energy barrier than for ammonia-borane addition, whilst we conclude that the THF-based dehydrogenation of "**2b**" is slightly endothermic. In Fe-mediated catalyst **2**, the dehydrogenation process is lower in the gas phase, whereas endothermic in nature in solvent. The difference of these barriers can be explained by NPA charges on -Fe(H) in **2b-TS2**; the metal atom carries a slightly positive charge (+0.069e) (cf. Table 2). For both catalysts, **AB**-addition step was found to more energetically favorable; de-hydrogenation exhibited somewhat higher energetic values.

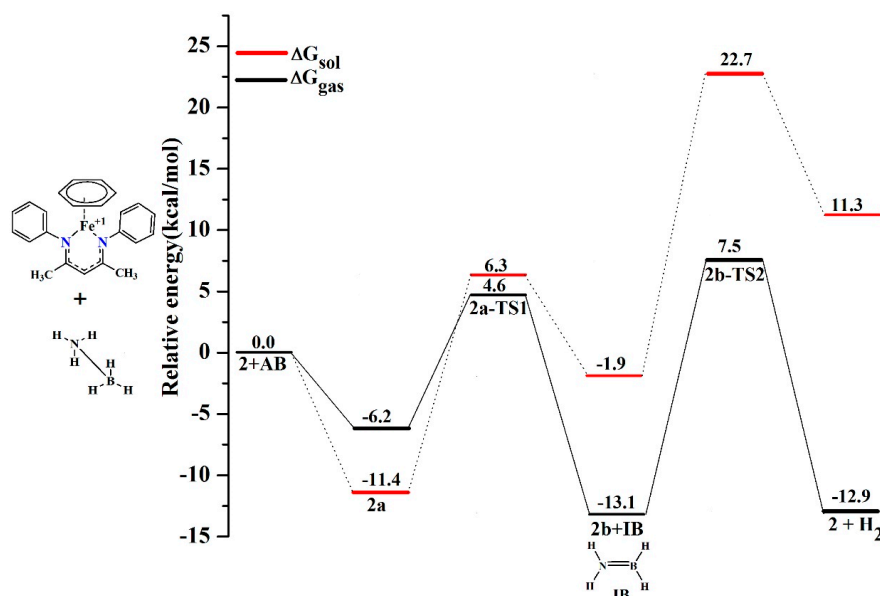


Figure 4. Profile of the reaction coordinate for addition of catalyst "**2**" to "**AB**" via "**2a-TS1**" to form "**2b**" and H_2 release from the dihydrogenated product "**2b**". The gas-phase relative Gibbs free energies (—) and in-solvent relative energies (---) are given in kcal/mol.

6. Mechanism Involving Metal Catalyst “3” and “4” Addition to Ammonia Borane

We have designed metal catalysts **3** and **4** based on experimental insights, particularly **3**, which was designed based on the previously reported Ru catalyst [17]. The reactions were carried out using bifunctional η^6 -arene β -diketiminato ruthenium catalyst in different substituted THF solvent molecules; the bifunctional η^6 -arene β -diketiminato ruthenium catalyst loses the phenyl and the metal ($M \dots \pi$) contacts, and the resultant product is *thiol* (-SCH₃)-substituted metal catalyst **3** [47]. We are interested in seeing how the reaction pathways proceed and how energies vary for the designed catalysts. Here, the arene ring is substituted by a THF molecule: we wish to ascertain how THF molecules affect the energy barriers and the ease, or difficulty, of releasing H₂. We have also designed via DFT the iron-based analogue **4**. In this catalyst, we switch the metal atom Ru to Fe to see how the energetics vary and to study the charge on the metal and the β -carbon and -NH and -BH centers, determining how the reaction-energy barriers change.

Firstly, we have designed the catalysts **3** and **4** without the THF solvent molecule coordinated at the metal center. We attempted ammonia-borane addition to the metal catalyst, but all of our extensive efforts failed due to a panoply of stationary points on the potential energy surface. This indicated that the solvent molecule plays an important role in stabilizing the metal catalyst, underlying our previous observations on the importance in some situations of explicit representation of the solvent [3]. We have considered various Ru...THF coordination conformations for the THF molecule position; we chose the most stable and lowest-energy configurations. We carried out ammonia-borane addition calculations with the THF coordinated to the metal center for catalyst **3** as a starting point, given that we suspected this explicit presence of a non-innocent THF molecule would serve to reduce the charge on the metal center ($M \rightarrow O$ in THF), thus stabilizing the catalyst and promoting **AB** addition.

The reaction proceeds by the same mechanism [17] which involves metal catalyst **3** and **4** associating with ammonia borane to form an associate complex **3a** and **4a** via N...H and B...H interactions, and afterwards the proton transfers from the -HN atom of **AB** to the β -carbon site, and the boron hydride -B to M (metal site) to produce the dihydrogenated products **3b** and **4b**. Finally, H₂ is released from the hydrogenated products (**3b** and **4b**) and catalysts **3** and **4** regenerate for the next catalytic cycle. All of the relative-energy graphs and optimized structures for Ru metal catalyst **3** are shown in Figures 5 and 6, respectively, whilst those for the Fe-based catalyst **4**, are shown in Figures S1 and S2, respectively (cf. Supplementary Materials), and the corresponding NPA charges are specified in Table 3.

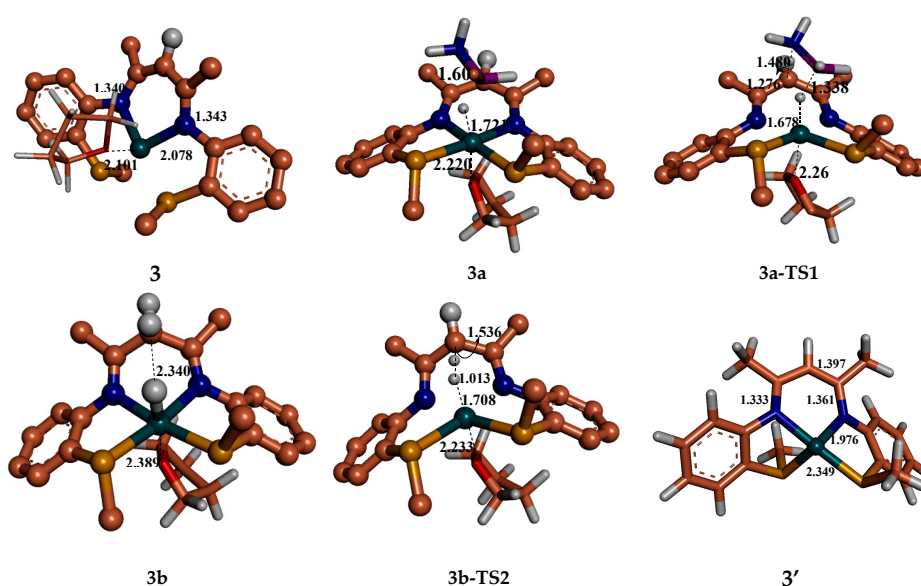


Figure 5. Significant optimized geometries (of important stationary points for **AB** addition to the Ru metal catalyst **3**). Important hydrogen atoms are shown.

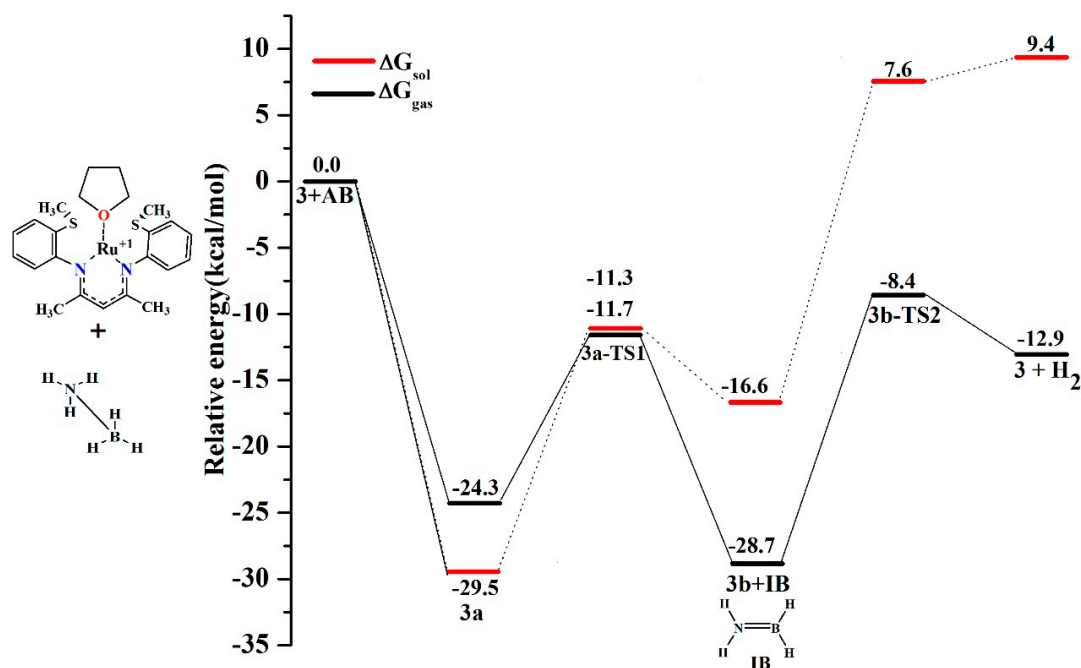


Figure 6. Reaction-coordinate profile of addition of catalyst “3” to “AB” via “3a” association complex and “3a-TS1” to form “3b” and H₂ release from the dihydrogenated product “3b”. Relative Gibbs free energies gas-phase (—) and solvated bases (—) are specified in kcal/mol.

3a’s structure demonstrates the closest contact, 1.721 Å, between AB and the catalyst 3 (cf. Figure 5); this is mediated by the (B)H-Ru interaction. In the association complex 3a, the AB interaction is in closer contact with catalyst 3 than the reported Ru meta-association complex [17]. This may be observed clearly from the relative energy: the relative energetic values are more favorable than for the previously reported catalyst [17]. However, 3a evinces an added, but markedly weaker, N(H)-C(β) interaction taking place over 2.26 Å. Again, solvation-effect adjustments to energetics were also handled by the PCM-THF approach. In essence, these calculations conclude that the formation of 3a from a combination of 3 + AB in solvent is substantially less energetically favorable with a value of −29.5 kcal/mol.

Table 3. NPA charges involved in metal catalysts “3” and “4” in reaction complexes and TSs (B, H, N, H, C, and M) and TS2’s corresponding intermediate (C(β), M(Ru, Fe), H(Cβ), H(M)). Transition-state imaginary frequencies (ω_i) given in cm^{−1}.

Structure	B	H(B)	N	H(N)	C(β)	M(Ru)	THF(O)	ω _i
3	-	-	-	-	−0.395	0.110	−0.525	-
3a	−0.011	−0.007	−0.963	0.463	0.304	−0.240	−0.546	-
3a-TS1	0.096	−0.020	−1.113	0.396	−0.646	−0.285	−0.555	−880.6i
	C(β)	M(Ru)	H(Cβ)	H(M)	THF(O)	ω _i	-	-
3b	−0.565	−0.588	0.320	0.054	−0.574	-	-	-
3b-TS2	−0.576	−0.403	0.259	0.052	−0.555	−1281.9i	-	-
	B	H(B)	N	H(N)	C(β)	M(Fe)	THF(O)	ω _i
4	-	-	-	−0.430	0.382	−0.588	−0.430	-
4a	−0.024	−0.076	−0.974	0.459	−0.468	0.151	−0.597	-
4a-TS1	0.060	−0.097	−1.121	0.391	−0.648	0.079	−0.597	−627.3i
	C(β)	M(Ru)	H(Cβ)	H(M)	THF(O)	ω _i	-	-
4b	−0.573	−0.365	0.328	−0.043	−0.587	-	-	-
4b-TS2	−0.592	−0.132	0.274	−0.443	−0.580	−1278.6i	-	-

Interestingly, the designed Fe-based catalyst **4** follows a similar tendency; for the formation of **4a** from **4** + **AB** (cf. Figure S1), we have calculated the energy pathways for catalyst **4**. The corresponding reaction pathway is shown in the Supporting Information, alongside the relative-energy differences. For catalyst **4**, **AB** addition is highly energetically favorable and thermodynamically stable, involving a higher activation energy barrier. The $4a \rightarrow TS1$ exhibits a higher activation-energy barrier compared to the earlier-reported catalyst [17]. These transition states are thermodynamically stable. The solvent adopts an important role in these types of systems: the in-solvent reactions appear to be endothermic (cf. Figure 6 and Figure S1). Examining the charge on the O atom of the THF molecule, from initially on the metal catalyst ($-0.505e$) to the end of the reaction, charge accumulation thereon is enhanced (**3a**: $-0.540e$, **3a-TS1**: $-0.552e$, and **3b**: $-0.576e$).

In the mono-hydride β -diimine complex, **3b** and **4b**, the respective distances between the two hydrogen atoms are 2.34 and 2.21 Å, suggesting that there is a $H^{\delta+}-H^{\delta-}$ interaction at play; this deviates somewhat, however, from the already-proposed Ru catalyst [17]. The dehydrogenation of the complex "**3b**" exhibits a moderately lower energy barrier vis-à-vis the previously-explored catalyst, whilst dehydrogenation of "**3b**" in THF is concluded to be more endothermic. Amongst catalysts **3** and **4**, the Fe-based one has a dehydrogenation step for **4-TS2** which seems to exhibit a more favorable activation energy than **3-TS2** and the previously-reported Ru catalyst [17]. One exception to this trend lies in the reaction-energy barrier of **4-TS2**: this difference for **4-TS2** may be rationalised from its differing NPA charges on the atoms involved in the transition state (cf. Table 3).

7. Conclusions

We have designed in silico four different catalysts to explore their reaction pathways using the wB97XD functional. THF-solvation effects were modelled using the PCM model. For iron-substituted catalysts, the dehydrogenation energy-barriers are more favorable than for their Ru-based counterparts. wB97XD-computed values for ammonia-borane addition to the metal catalyst suggest greater energetic favorability, whereas for dehydrogenation, this is less so. From the perspective of DFT with improved treatment of dispersion, the designed low-spin Fe-based catalysts appear more effective for hydrogen storage in ammonia borane than Ru-based catalysts; these may be synthetically and economically more viable hydrogen-storage candidates for the ammonia borane system, although further experimental efforts are needed to investigate this more thoroughly. Of course, it has now become widely accepted within the community that iron-based catalysis of this process is quite thermodynamically favorable, and this is consistent with the results of the present study. Therefore, a potential concern is that a reaction may have reversibility challenges if using iron-based catalysis. Further research into refining catalyst design beyond the proof-of-principle demonstration of the four studied in this work is warranted to make ammonia borane more viable as a practical, reversible hydrogen-storage medium; from this context, molecular simulation serves as an ideal 'prototyping' or 'screening' approach by which to pursue further experimental efforts in this regard.

Supplementary Materials: The following are available online at www.mdpi.com/2073-4344/7/5/140/s1. Figure S1: (a) Reaction-coordinate profile of addition of catalyst "**4**" to "**AB**" via **4-TS1** to form "**4b**" and (b) H_2 release from the dihydrogenated product "**4b**". Gas-phase relative free energies (kcal/mol) and relative free energies in THF solvent are also indicated (by red bars). Figure S2: Significant optimised geometries of important stationary points for the reaction coordinate of AB addition to Fe metal catalyst **4**. Important hydrogen atoms are shown for clarity.

Acknowledgments: This material is based upon works supported by Science Foundation Ireland (SFI) under Grant No. 07/SRC/B1160 and Grant No. 15/ERC/I3142. BS acknowledges gratefully the financial support of the Natural Science Foundation of China (No. 21650110464). We thank Enterprise Ireland, as well as SFI and the Irish Centre for High-End Computing for the provision of high-performance computing facilities.

Author Contributions: S.B. and N.J.E. conceived the computational study, on foot of higher-level and motivational hydrogen-storage discussions with J.M.D.M., with much detailed system-specific scientific advice and experimental-background input from A.D.P. S.B. performed the simulation and analysis, with input from N.J.E. All authors contributed to preparing the manuscript.

Conflicts of Interest: The authors declare no conflict of interest.

References

1. Coontz, R.; Hanson, B. Not So Simple. *Science* **2004**, *305*, 957. [[CrossRef](#)]
2. Crabtree, G.W.; Dresselhaus, M.S.; Buchanan, M.V. The Hydrogen Economy. *Phys. Today* **2004**, *57*, 39–44. [[CrossRef](#)]
3. Bandaru, S.; English, N.J.; MacElroy, J.M.D. Implicit and explicit solvent models for modeling a bifunctional arene ruthenium hydrogen-storage catalyst: A classical and ab initio molecular simulation study. *J. Comput. Chem.* **2014**, *35*, 683–691. [[CrossRef](#)] [[PubMed](#)]
4. Nguyen, M.T.; Nguyen, V.S.; Matus, M.H.; Gopakumar, G.; Dixon, D.A. Molecular Mechanism for H₂ Release from BH₃NH₃, Including the Catalytic Role of the Lewis Acid BH₃. *J. Phys. Chem. A* **2007**, *111*, 679–690. [[CrossRef](#)] [[PubMed](#)]
5. Aska, C.A.; Temple, K.; Lough, A.J.; Manners, I. Transition Metal-Catalyzed Formation of Boron–Nitrogen Bonds: Catalytic Dehydrocoupling of Amine–Borane Adducts to Form Aminoboranes and Borazines. *J. Am. Chem. Soc.* **2003**, *125*, 9424–9434.
6. Stephens, F.H.; Baker, R.T.; Matus, M.H.; Grant, D.J.; Dixon, D.A. Acid Initiation of Ammonia–Borane Dehydrogenation for Hydrogen Storage. *Angew. Chem.* **2007**, *119*, 649–652. [[CrossRef](#)]
7. Stephens, F.H.; Baker, R.T.; Matus, M.H.; Grant, D.J.; Dixon, D.A. Acid Initiation of Ammonia–Borane Dehydrogenation for Hydrogen Storage. *Angew. Chem. Int. Ed.* **2007**, *46*, 746–749. [[CrossRef](#)] [[PubMed](#)]
8. Keaton, R.J.; Blacquiere, J.M.; Baker, R.T. Base Metal Catalyzed Dehydrogenation of Ammonia–Borane for Chemical Hydrogen Storage. *J. Am. Chem. Soc.* **2007**, *129*, 1844–1845. [[CrossRef](#)] [[PubMed](#)]
9. Chen, Y.; Fulton, J.L.; Linehan, J.L.; Autrey, T. In Situ XAFS and NMR Study of Rhodium-Catalyzed Dehydrogenation of Dimethylamine Borane. *J. Am. Chem. Soc.* **2005**, *127*, 3254–3255. [[CrossRef](#)] [[PubMed](#)]
10. Clark, T.J.; Russell, C.A.; Manners, I. Homogeneous, Titanocene-Catalyzed Dehydrocoupling of Amine–Borane Adducts. *J. Am. Chem. Soc.* **2006**, *128*, 9582–9583. [[CrossRef](#)] [[PubMed](#)]
11. Denney, M.C.; Pons, V.; Hebden, T.J.; Heinekey, D.M.; Goldberg, K.J. Efficient Catalysis of Ammonia Borane Dehydrogenation. *J. Am. Chem. Soc.* **2006**, *128*, 12048–12049. [[CrossRef](#)] [[PubMed](#)]
12. Bluhm, M.E.; Bradley, M.G.; Butterick, R.; Kusari, U.; Sneddon, L.G. Amineborane-Based Chemical Hydrogen Storage: Enhanced Ammonia Borane Dehydrogenation in Ionic Liquids. *J. Am. Chem. Soc.* **2006**, *128*, 7748–7749. [[CrossRef](#)] [[PubMed](#)]
13. Balazs, N.; Brahim, K.; Claude, G.; Veszprémi, T. Differences Between Amine- and Phosphine-Boranes: Synthesis, Photoelectron Spectroscopy, and Quantum Chemical Study of the Cyclopropylic Derivatives. *Inorg. Chem.* **2010**, *49*, 4854–4864.
14. Swinnen, S.; Nguyen, V.S.; Nguyen, M.T. Hydrogen release from ammonia borane and derivatives in the presence of a ruthenium complex incorporating cooperative PNP ligands. *Chem. Phys. Lett.* **2011**, *513*, 195–200. [[CrossRef](#)]
15. Swinnen, S.; Nguyen, V.S.; Nguyen, M.T. Theoretical study of the hydrogen release mechanism from a lithium derivative of ammonia borane, LiNH₂BH₃–NH₃BH₃. *Chem. Phys. Lett.* **2011**, *517*, 22–28. [[CrossRef](#)]
16. Schreiber, D.F.; O'Connor, C.; Grave, C.; Ortin, Y.; Müller-Bunz, H.; Phillips, A.D. Application of β-Diketiminato Arene-Substituted Ru(II) Complexes in Highly Efficient H₂ Dehydrocoupling of Amine Boranes. *ACS Catal.* **2012**, *2*, 2505–2511. [[CrossRef](#)]
17. Bandaru, S.; English, N.J.; Phillips, A.D.; MacElroy, J.M.D. Towards the design of novel boron- and nitrogen-substituted ammonia-borane and bifunctional arene ruthenium catalysts for hydrogen storage. *J. Comput. Chem.* **2014**, *35*, 891–903. [[CrossRef](#)] [[PubMed](#)]
18. Boddien, A.; Mellmann, D.; Gärtner, F.; Jackstell, R.; Junge, H.; Dyson, P.J.; Laurenczy, G.; Ludwig, R.; Beller, M. Efficient Dehydrogenation of Formic Acid Using an Iron Catalyst. *Science* **2011**, *333*, 1733–1736. [[CrossRef](#)] [[PubMed](#)]
19. Boddien, A.; Grtner, F.; Jackstell, R.; Junge, H.; Spannenberg, A.; Baumann, W.; Ludwig, R.; Beller, M. ortho-Metalation of Iron(0) Tribenzylphosphine Complexes: Homogeneous Catalysts for the Generation of Hydrogen from Formic Acid. *Angew. Chem. Int. Ed.* **2010**, *49*, 8993–8996. [[CrossRef](#)] [[PubMed](#)]
20. Yan, J.M.; Zhang, X.B.; Han, S.; Shioyama, H.; Xu, Q. Iron-Nanoparticle-Catalyzed Hydrolytic Dehydrogenation of Ammonia Borane for Chemical Hydrogen Storage. *Angew. Chem. Int. Ed.* **2008**, *47*, 2287–2289. [[CrossRef](#)] [[PubMed](#)]

21. Baker, R.T.; Gordon, J.C.; Hamilton, C.W.; Henson, N.J.; Lin, P.H.; Maguire, S.; Murugesu, M.; Scott, B.L.; Smythe, N.C. Iron Complex-Catalyzed Ammonia–Borane Dehydrogenation. A Potential Route toward B–N-Containing Polymer Motifs Using Earth-Abundant Metal Catalysts. *J. Am. Chem. Soc.* **2012**, *134*, 5598–5609. [[CrossRef](#)] [[PubMed](#)]
22. Douglas, T.M.; Chaplin, A.B.; Weller, A.S.; Yang, X.; Hall, M.B. Monomeric and Oligomeric Amine–Borane σ -Complexes of Rhodium. Intermediates in the Catalytic Dehydrogenation of Amine–Boranes. *J. Am. Chem. Soc.* **2009**, *131*, 15440–15456. [[CrossRef](#)] [[PubMed](#)]
23. Kumar, A.; Priest, I.K.; Hooper, T.N.; Weller, A.S. Variable coordination modes and catalytic dehydrogenation of *B*-phenyl amine–boranes. *Dalton Trans.* **2016**, *45*, 6183–6195. [[CrossRef](#)] [[PubMed](#)]
24. Douglas, T.M.; Chaplin, A.B.; Weller, A.S. Amine–Borane σ -Complexes of Rhodium. Relevance to the Catalytic Dehydrogenation of Amine–Boranes. *J. Am. Chem. Soc.* **2008**, *130*, 14432–14433. [[CrossRef](#)] [[PubMed](#)]
25. Kumar, A.; Ishibashi, J.S.A.; Hooper, T.N.; Mikulas, T.C.; Dixon, D.A.; Liu, S.-Y.; Weller, A.S. The Synthesis, Characterization and Dehydrogenation of Sigma-Complexes of BN-Cyclohexanes. *Chem. Eur. J.* **2016**, *22*, 310–322. [[CrossRef](#)] [[PubMed](#)]
26. Butera, V.; Russo, N.; Sicilia, E. The Role of Chelating Phosphine Rhodium Complexes in Dehydrocoupling Reactions of Amine–Boranes: A Theoretical Investigation Attempting To Rationalize the Observed Behaviors. *ACS Catal.* **2014**, *4*, 1104–1113. [[CrossRef](#)]
27. Butera, V.; Russo, N.; Sicilia, E.A. Hydrogen Release from Dialkylamine–Boranes Promoted by Mg and Ca Complexes: A DFT Analysis of the Reaction Mechanism. *Chem. Eur. J.* **2014**, *20*, 5967–5976. [[CrossRef](#)] [[PubMed](#)]
28. Li, H.; Hall, M.B. Role of the Chemically Non-Innocent Ligand in the Catalytic Formation of Hydrogen and Carbon Dioxide from Methanol and Water with the Metal as the Spectator. *J. Am. Chem. Soc.* **2015**, *137*, 12330–12342. [[CrossRef](#)] [[PubMed](#)]
29. Alberico, E.; Lennox, A.J.J.; Vogt, L.K.; Jiao, H.; Baumann, W.; Drexler, H.-J.; Nielsen, M.; Spannenberg, A.; Checinski, M.P.; Junge, H. Unravelling the Mechanism of Basic Aqueous Methanol Dehydrogenation Catalyzed by Ru–PNP Pincer Complexes. *J. Am. Chem. Soc.* **2016**, *138*, 14890–14904. [[CrossRef](#)] [[PubMed](#)]
30. Jinga, Y.; Chena, X.; Yang, X. Theoretical study of the mechanism of ruthenium catalyzed dehydrogenation of methanol–water mixture to H₂ and CO₂. *J. Org. Organomet. Chem.* **2016**, *820*, 55–61. [[CrossRef](#)]
31. Zhao, Y.; Schultz, N.E.; Truhlar, D.G. Design of Density Functionals by Combining the Method of Constraint Satisfaction with Parametrization for Thermochemistry, Thermochemical Kinetics, and Noncovalent Interactions. *J. Chem. Theory Comput.* **2006**, *2*, 364–382. [[CrossRef](#)] [[PubMed](#)]
32. Grimme, S. Semiempirical GGA-type density functional constructed with a long-range dispersion correction. *J. Comput. Chem.* **2006**, *27*, 1787–1799. [[CrossRef](#)] [[PubMed](#)]
33. Becke, A.D. Density-functional thermochemistry. V. Systematic optimization of exchange–correlation functionals. *J. Chem. Phys.* **1997**, *107*, 8554–8560. [[CrossRef](#)]
34. Chai, J.D.; Gordon, M. Long-range corrected hybrid density functionals with damped atom–atom dispersion corrections. *Phys. Chem. Chem. Phys.* **2008**, *10*, 6615–6620. [[CrossRef](#)] [[PubMed](#)]
35. Wu, Q.; Yang, W.T. Empirical correction to density functional theory for van der Waals interactions. *J. Chem. Phys.* **2002**, *116*, 515–524. [[CrossRef](#)]
36. Frisch, M.J.; Trucks, G.W.; Schlegel, H.B.; Scuseria, G.E.; Robb, M.A.; Cheeseman, J.R.; Scalmani, G.; Barone, V.; Mennucci, B.; Petersson, G.A.; et al. *Gaussian 09, Revision A.1*; Gaussian, Inc.: Wallingford, CT, USA, 2009.
37. Nicklass, A.; Dolg, M.; Stoll, H.; Preuss, H. Ab initio energy-adjusted pseudopotentials for the noble gases Ne through Xe: Calculation of atomic dipole and quadrupole polarizabilities. *J. Chem. Phys.* **1995**, *102*, 8942–8952. [[CrossRef](#)]
38. Ditchfield, R.; Hehre, W.J.; Pople, J.A. Self–Consistent Molecular Orbital Methods. XII. Further Extensions of Gaussian–Type Basis Sets for Use in Molecular Orbital Studies of Organic Molecules. *J. Chem. Phys.* **1971**, *54*, 2257–2261. [[CrossRef](#)]
39. Woon, D.E.; Dunning, T.H., Jr. Gaussian basis sets for use in correlated molecular calculations. III. The atoms aluminum through argon. *J. Chem. Phys.* **1993**, *98*, 1358–1371. [[CrossRef](#)]
40. Carpenter, J.E.; Weinhold, F. Analysis of the geometry of the hydroxymethyl radical by the “different hybrids for different spins” natural bond orbital procedure. *J. Mol. Struct. (THEOCHEM)* **1988**, *169*, 41–62. [[CrossRef](#)]

41. Miertus, S.; Scrocco, E.; Tomasi, J. Electrostatic interaction of a solute with a continuum. A direct utilization of AB initio molecular potentials for the prevision of solvent effects. *Chem. Phys.* **1981**, *55*, 117–129. [[CrossRef](#)]
42. Cammi, R.; Tomasi, J. Remarks on the use of the apparent surface charges (ASC) methods in solvation problems: Iterative versus matrix-inversion procedures and the renormalization of the apparent charges. *J. Comput. Chem.* **1995**, *16*, 1449–1458. [[CrossRef](#)]
43. English, N.J.; MacElroy, J.M.D. Atomistic simulations of liquid water using Lekner electrostatics. *Molec. Phys.* **2002**, *100*, 3753–3769. [[CrossRef](#)]
44. English, N.J. Effect of electrostatics techniques on the estimation of thermal conductivity via equilibrium molecular dynamics simulation: Application to methane hydrate. *Mol. Phys.* **2008**, *106*, 1887–1898. [[CrossRef](#)]
45. Phillips, A.D.; Laurency, G.; Scopelliti, R.; Dyson, P.J. Facile, Thermoreversible Cycloaddition of Small Molecules to a Ruthenium(II) Arene β -Diketiminato. *Organometallics* **2007**, *26*, 1120–1134. [[CrossRef](#)]
46. Ledger, A.E.W.; Ellul, C.E.; Mahon, M.F.; Williams, J.M.J.; Whittlesey, M.K. Ruthenium Bidentate Phosphine Complexes for the Coordination and Catalytic Dehydrogenation of Amine- and Phosphine-Boranes. *Chem. Eur. J.* **2011**, *17*, 8704–8713. [[CrossRef](#)] [[PubMed](#)]
47. Phillips, A.D.; Grave, C.; Singh, G.; O'Connor, C.; Khlebnikov, C. Catalyst and Process for the Production of Hydrogen from Ammonia Boranes. International Patent WO2014174465A3, 23 April 2014.



© 2017 by the authors. Licensee MDPI, Basel, Switzerland. This article is an open access article distributed under the terms and conditions of the Creative Commons Attribution (CC BY) license (<http://creativecommons.org/licenses/by/4.0/>).